Journal of
Applied Crystallography

ISSN 0021-8898

Received 23 April 2004
Accepted 30 June 2004

X-ray imaging with ultra-small-angle X-ray scattering as a contrast mechanism

L. E. Levine* and G. G. Long

Materials Science and Engineering Laboratory, National Institute of Standards and Technology, Gaithersburg, MD 20899, USA. Correspondence e-mail: lyle.levine@nist.gov

A new transmission X-ray imaging technique using ultra-small-angle X-ray scattering (USAXS) as a contrast mechanism is described. USAXS imaging can sometimes provide contrast in cases where radiography and phase-contrast imaging are unsuccessful. Images produced at different scattering vectors highlight different microstructural features within the same sample volume. When used in conjunction with USAXS scans, USAXS imaging provides substantial quantitative and qualitative three-dimensional information on the sizes, shapes and spatial arrangements of the scattering objects. The imaging technique is demonstrated on metal and biological samples.

1. Introduction

Small-angle scattering (SAS) is a widely used experimental technique that typically provides quantitative statistical volume-averaged microstructural information from bulk specimens (Windsor, 1988). However, conducting a quantitative small-angle X-ray scattering analysis requires *a priori* information on the shapes and electron densities (*i.e.* chemistry) of the scattering objects within the sample. Also, SAS provides almost no information on how the scattering objects are distributed in the scattering volume. Ultra-small-angle X-ray scattering (USAXS) imaging greatly expands the usefulness of SAS in four main ways. First, it provides direct images of the shapes and three-dimensional arrangement of the scattering objects. Second, the local scattering intensity can be measured as a function of scattering vector, **q** (where $|\mathbf{q}| = (4\pi/\lambda)\sin\theta$, λ is the X-ray wavelength, and 2θ is the scattering angle), by comparing images produced at different **q**'s. From these q-dependent scattering data, it becomes possible to extract shape and size information even when the scattering objects are smaller than the spatial resolution of the images (although determination of their location is still limited by the resolution). Third, USAXS imaging greatly extends the size range over which microstructural information can be obtained. Our USAXS instrument (Ilavsky *et al.*, 2004) measures real-space structures from about 1 nm to a little over 1 μm in size. USAXS imaging extends this range to millimetre-sized structures by directly imaging them. Fourth, USAXS imaging can identify the source of the observed scattering and thus verify that the measured intensity arises from the desired microstructural features. For example, SAXS analyses of large-grain metallic samples are often hampered by contamination from double Bragg diffraction from opportunistically oriented grains or scattering from damaged surfaces. By directly imaging the sources of the measured X-ray intensity, USAXS imaging can identify such artifacts so that corrective action can be taken to eliminate them. Although potentially useful in its own right, the real strength of USAXS imaging is likely to lie in its complementary use with USAXS.

The SAS contrast mechanism provides inherently high-contrast images of the density variations within a sample. This is because the only X-rays that contribute to the image are those produced by SAS at the selected **q**. Thus, a single scattering object in a sample matrix of uniform density will be readily visible as the only source of X-ray intensity, even when the sample thickness varies considerably. This is in contrast to radiography and phase-contrast imaging, where variations in sample thickness contribute directly to the image intensity.

As a simple example of how USAXS and USAXS imaging can work together, consider a set of scattering objects distributed heterogeneously within a sample. If the objects are smaller than the spatial resolution of the imaging system, the scattered X-rays will still appear in the image as unresolved features. By comparing images obtained from different values of **q**, the local **q** dependence (at low **q**) can be measured and information concerning the sizes and shapes of the objects can be extracted.

2. Experimental procedure

The experiments reported here were conducted using the UNICAT sector 33 USAXS instrument at the Advanced Photon Source (Ilavsky *et al.*, 2004). This Bonse–Hart-type instrument (shown schematically in Fig. 1) is installed on an undulator beamline after a double-crystal monochromator (for photon energy selection) and two mirrors (for harmonic rejection). It delivers $\sim 10^{12}$ photons s^{-1} mm^{-2} at the sample position, in the energy range of incident photons from 7 to 17 keV. The size of the X-ray beam (typically $\sim 0.4 \times 2.0$ mm) is controlled by incident beam slits, after which a Si $\langle 111 \rangle$ channel-cut crystal pair acts as a collimator. Two to six reflections are commonly used. A windowless ion chamber

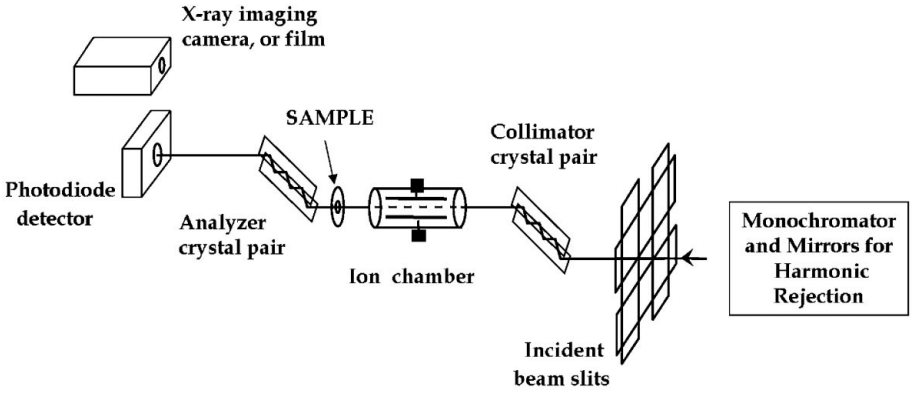

Figure 1
Schematic diagram of the USAXS instrument.

after the collimator monitors the photon flux incident on the sample. After the sample, a crystal pair (the analyzer) serves as an angular filter that selects **q**. Both Si ⟨111⟩ and Ge ⟨111⟩ crystal pairs have been used for the analyzer. The angular (or q) resolution of the analyzer is given by the width of its rocking curve. For Si ⟨111⟩ at a photon energy of 8.94 keV, we have a measured half width at half-maximum (HWHM) of 0.0007°.

A USAXS scan of the sample is acquired by rotating the analyzer and recording the scattered photons detected by a photodiode that is linear over ten decades of X-ray intensity. By making positional corrections for the detector and analyzer during a scan, the accessible q range is approximately 1.0×10^{-4} to 3.0 Å^{-1}. During alignment, the photodiode detector is replaced by an intensified X-ray imaging camera (8 μm pixel size) which allows direct radiographic inspection of the sample.

Before the USAXS images are acquired, the sample is viewed radiographically to check for pinholes or other sample regions that we might want to avoid. After this, USAXS scans are measured. These USAXS data provide useful information on the relevant length scales within the sample microstructure, thus allowing appropriate values of **q** for the imaging to be determined. USAXS images are formed by rotating the (non-dispersive) analyzer to a selected **q**, and replacing the photodiode detector with an imager (either a high-resolution digital X-ray camera or a nuclear emulsion plate). Thus, the entire USAXS image is acquired in a single exposure and no raster scanning of the beam across the sample is required.

Since the scattering intensity generally drops off rapidly with increasing q, USAXS imaging becomes more difficult at large q. The accessible q range is determined by the incident-beam intensity, the sample absorption, the sensitivity of the imaging system, and how rapidly the scattering intensity decreases with q. As a typical example, with nuclear emulsion plates, we have successfully imaged voids in Cu for $0.00022 \text{ Å}^{-1} \leq q \leq 0.003 \text{ Å}^{-1}$. In terms of intensity, the large-q limit has approximately 5.0×10^{-6} of the transmitted intensity at $q = 0$. With our high-resolution X-ray camera, typical exposure times at low q are well under a second. Typically, filters are used to reduce the incident beam intensity, thereby increasing the exposure time to approximately 10 s for averaging over beam fluctuations. We are limited to a maximum q of about 0.0018 Å^{-1} for similar samples. At larger q, exposure times become greater than two hours and thermal noise in the camera becomes significant. Thus, for most of the samples we have examined, our USAXS imaging instrument has an effective q range of about one decade. In strongly scattering samples where the scattering drops off slower than q^{-4}, the accessible range can be much larger.

An individual USAXS image contains two-dimensional rather than three-dimensional information on the positions of the scattering objects. However, since rotation of the sample about **q** does not affect the USAXS, we use such rotations to produce stereo (three-dimensional) USAXS images of the scattering microstructures as well as rotation sequences of up to several hundred images. In principle, a full three-dimensional tomographic reconstruction should be feasible.

3. Connections to radiography and diffraction enhanced imaging

The earliest, and most commonly used, X-ray imaging technique is radiography, which uses absorption as the contrast mechanism. Phase-sensitive techniques such as 'diffraction enhanced imaging' (DEI) (Chapman *et al.*, 1997) are currently receiving considerable attention (Fitzgerald, 2000) for their potential to augment or complement the radiographic techniques. Although USAXS imaging is distinct from both radiographic and phase-contrast imaging, all three techniques are closely related and a brief comparison of the underlying mechanisms is useful. In this discussion, phase-contrast techniques which exploit the coherent fraction of the incident beam will not be included.

The most significant operational factor distinguishing the three imaging techniques is the angle that the detected X-rays make with respect to the incident beam. Radiographic contrast comes from variations in the transmittance of the sample at $q = 0$. DEI images are taken at the peak of the analyzer's rocking curve and at each of the half-width positions. Finally, USAXS imaging uses X-rays that are scattered at much larger angles. The relevant interaction processes within the sample include photoelectric absorption, diffraction by local atomic or larger structures, elastic scattering and inelastic scattering. The relative magnitude of these effects depends upon a number of factors intrinsic to the sample as well as the X-ray wavelength and the angle at which the observation is made.

We start with a description of the incident beam profile (no sample). The maximum beam intensity occurs at $q = 0$ and the intensity decreases monotonically with increasing angle. The details of this angular dependence and the possible appearance of side lobes depends upon the beamline design.

However, the angular dependence in at least one direction will generally follow the rocking curve of either the monochromator or any subsequent diffracting crystals. For our USAXS instrument, this situation is represented by a single measured curve, acquired with no sample, no absorbers, no slits, no windows and no physical beam stop in the beam, over eight decades or more in intensity.

With a sample in the beam, the measured intensity distribution (normalized by the sample transmission at $q = 0$ and in the absence of multiple scattering) closely follows the shape of the instrument function over the first decade or more of the analyzer rocking curve. After that, the slope decreases much less rapidly, as one records the elastic SAS. We refer to the angular region where the two spectra match as a 'virtual beam stop'. Within this angular range, we cannot measure the SAS because it is very small compared with the transmitted beam. The specific angle that defines the edge of the virtual beam stop depends upon several factors, including the width of the rocking curve and the SAS contrast of the sample features. USAXS imaging is always conducted outside this boundary where elastic SAS processes dominate; radiography and DEI are conducted well within this angle.

Behind the beam stop, photoelectric absorption is the primary process providing contrast for radiography. The dominant mechanism responsible for DEI contrast, whether it is refraction (Davis, 1994; Berk & Hardman-Rhyne, 1985) (von Nardroff) or small-angle scattering (Davis, 1994; Berk & Hardman-Rhyne, 1985) (the first Born approximation or the Rayleigh–Gans model) depends upon the sizes of the particles within the microstructure, the scattering length density $\Delta\rho$ (where $\Delta\rho$ is the difference in electron density between the scattering object and the matrix) and the wavelength of the incident radiation. Unified treatments of these phenomena (Davis, 1994; Berk & Hardman-Rhyne, 1985) have shown that small-angle scattering and refraction are simply different aspects of the same small-angle phenomenon.

Superficially, USAXS imaging bears a strong resemblance to DEI. Both techniques use parallel monochromatic X-ray beams in a transmission geometry and both angle-filter the transmitted beam using diffracting optics. After the beam passes through the sample, a single analyzer crystal is used in DEI to provide the angular filter. Images are taken at the peak of the analyzer's rocking curve and at each of the half-width positions so that an 'effective absorption' image and a 'phase contrast' image can be derived. Thus, in DEI, the half-width data includes both absorption and small-angle (or refraction) data and the small-angle (or refraction) data are examined only at extremely low q (inside our virtual beam stop). Flat fielding of the images is extremely important since the image features sit on top of the transmitted beam, which becomes a high-intensity background. The contrast of these features (given by their intensity relative to the background) decreases with object size since small-angle scattering from all except the largest objects will satisfy the Guinier approximation (Guinier & Fournet, 1955). Davis *et al.* (1995) pointed out that an optical system that is sensitive to the direction of propagation of the X-rays is also capable of phase-contrast imaging. The experimental design for such a system used a highly asymmetric Bonse–Hart geometry that allowed phase-contrast images to be obtained from a range of angles within the rocking curve of the analyzer crystals. In USAXS imaging, contrast is greater because all of the data are acquired at angles outside of the virtual beam stop where the intensity of the transmitted beam is much smaller than the small-angle data. USAXS imaging is thus a dark-field imaging technique in which the acquired X-rays are scattered at angles much larger than the rocking curve of the analyzer crystals. In the Davis *et al.* (1995) paper, the X-rays used to form the phase-contrast images are acquired at angles within this rocking curve. An additional advantage of USAXS imaging comes from our ability to acquire images within an angular range where the relative scattering intensity from individually imaged objects is size, shape and **q** dependent. Thus, taking multiple images of these objects at different scattering vectors gives us access to a large amount of additional structural data. The most significant drawback to USAXS imaging is the low photon flux at large **q**.

USAXS images often look very different from images that include an absorption component. In an absorption image of a sample containing two regions with substantially different electron densities, the X-ray intensity from the two regions will differ and the interface will be simply the place where the intensity changes. In a USAXS image of the same sample volume, the only X-rays coming from the sample will come from the interface where the scattering intensity will be proportional to difference in electron density squared. Another important visibility criterion is that USAXS imaging can only 'see' structures that have a component perpendicular to the scattering vector. For example, when looking at a circular crack produced by indentation, the part of the crack that is perpendicular to **q** will be most visible and the part that is parallel to **q** will be invisible.

4. Theoretical background

As with other imaging techniques, image interpretation requires an understanding of the image formation process. For USAXS imaging, the most important considerations are the q dependence of the scattering from individual objects, the imaging properties of the analyzer crystals, and the X-ray path length in the instrument. We now explain the role these factors play and follow this with a discussion of the scattering background and multiple scattering.

The q dependence of scattering from individual compact objects of constant electron density is well known (Windsor, 1988). In the large-q (Porod) region, the scattering intensity exhibits oscillations within a power-law envelope function with exponents of -4 for spheres, -2 for disks and -1 for rods. There is also a strong orientational dependence of SAS from individual non-spherical objects. Acquiring images over a range of q's and adjusting the exposure times according to the expected q dependence of the envelope function allows the scattering curve of each visible object to be determined. The slit-smeared geometry of the USAXS instrument effec-

tively increases the exponent of the above power laws by one (*e.g.* spheres would exhibit an exponent of −3 instead of −4). To avoid confusion, however, we will refer to the non-slit-smeared exponents unless otherwise stated.

For spherical objects of uniform density, the scattering function was given first by Rayleigh (1911) as

$$I(q) = (\Delta\rho)^2 V^2 \left[3\frac{\sin qr - qr\cos qr}{(qr)^3}\right]^2, \qquad (1)$$

where V is the volume and r is the radius. Fig. 2 shows this function for $r = 5$ μm and $\Delta\rho = 1$. The Porod approximation is usually considered valid for $qr > 3$ and this limit is indicated on the figure. For reasons that will be discussed below, Porod scattering almost always dominates over Guinier scattering in USAXS imaging, so our discussion will center on the Porod scattering. All of the individually distinguishable scattering objects we have studied so far have oscillation periods that are shorter than or comparable with our q resolution. The oscillations are therefore typically not visible and only the envelope function will be considered explicitly at this time.

The size dependence of the scattering also plays an important role. For example, at a fixed value of q within the Porod region of spherical particles, the total scattering intensity is proportional to r^2 (the surface area). Since the area of the spheres projected onto the image is also proportional to r^2, differently sized objects would be expected to have the same contrast on an image. However, this is only true if the objects are all in the Porod region. Consider USAXS images of two spherical objects of different sizes. Starting at a q where both objects are in the Porod region, let us slowly decrease q. As long as both objects remain in the Porod region, their scattering intensity will increase as q^{-4}. However, as qr approaches 1 for the smaller object, it enters the Guinier region and the scattering intensity increases much more slowly than q^{-4} (see Fig. 2). Thus, as q becomes smaller, the scattering intensity from the smaller sphere increases more slowly than the larger one that remains within the Porod region. Thus, decreasing q has the effect of 'removing' the smaller scattering objects from the image. This is the reason for our earlier statement that the imaging contrast of very small objects in DEI is decreased relative to that of the larger objects. At the half-width positions of the rocking curve where DEI is used, the large objects are in their Porod region and thus exhibit a much higher contrast than the smaller objects that are in their Guinier region.

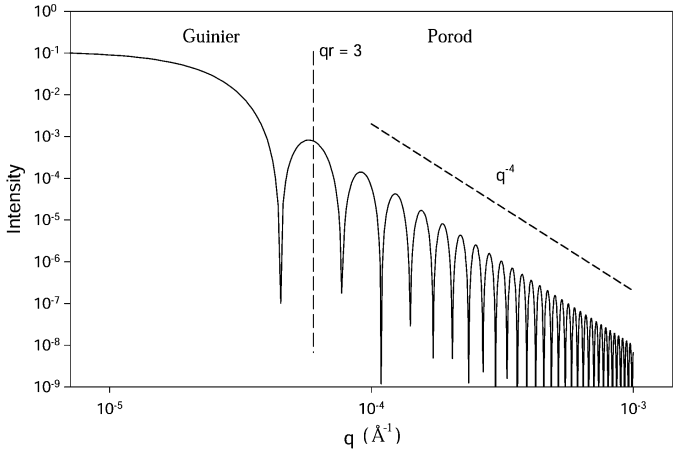

Figure 2
Theoretical small-angle scattering function for a sphere of 10 μm diameter.

We now consider the point-spread function (PSF) for our optical system. This is equivalent to considering a single point source at the sample position and asking what the image of this point would look like on the detector after passing through the X-ray optics. PSFs are commonly used to characterize both visible light (Hecht & Zajac, 1979) and X-ray (Davis, 1996) imaging systems. As mentioned above, USAXS imaging uses a slit-smeared geometry where the acceptance window for the scattered X-rays is very narrow in the direction perpendicular to the analyzer crystals (defining $q_\perp$) but is essentially unrestricted in the direction parallel to the crystals (defining $q_\parallel$). This acceptance window is shown in Fig. 3. In the $q_\perp$ direction, it is possible to derive an approximate PSF from the kinematic Takagi–Taupin equations for perfect crystals (Davis, 1996). In this paper, however, we approximate the PSF by using the directly measured rocking curve from the analyzer crystals to obtain the angular dependence, and then propagate this function through the geometry of our optical system. Thus, in the $q_\perp$ direction, the angular dependence of the PSF is given by the rocking curve that has a measured HWHM of 0.0007° with ⟨111⟩ Si analyzer crystals and a photon energy of 8.94 keV. At a sample-to-detector distance of 5.8 cm, the PSF would have an approximately Gaussian intensity distribution with an HWHM of 0.7 μm in the perpendicular direction (see Fig. 4*a*).

Parallel to the analyzer crystals (see Fig. 4*b*) there is no rocking curve to limit the angular spread of the image, and the divergence is limited primarily by the q dependence of the scattering objects. For a given image, $q_\perp$ is fixed by the analyzer orientation. As we allow $q_\parallel$ to vary, the combined scattering vector, $q_c = (q_\perp^2 + q_\parallel^2)^{1/2}$, increases from its minimum value of $q_\perp$ at $q_\parallel = 0$, causing the scattering intensity to decrease. For Porod scattering from spherical objects, the q^{-4} scattering results in a normalized intensity distribution of $I/I(q = q_\perp) = q_\perp^4/(q_\perp^2 + q_\parallel^2)^2$. For example, if $q_\perp = 1.3 \times 10^{-4}$ Å^{-1}, then the scattering will drop to half of its original intensity at $q_\parallel = 8.5 \times 10^{-5}$ Å^{-1}, which corresponds to an angle of 0.001°. This angular spread would produce an image with an

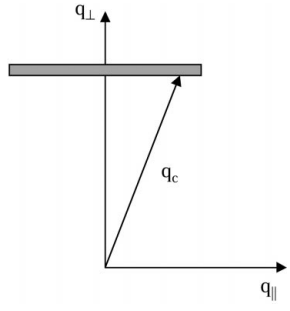

Figure 3
Definitions for the slit-smeared geometry in reciprocal space.

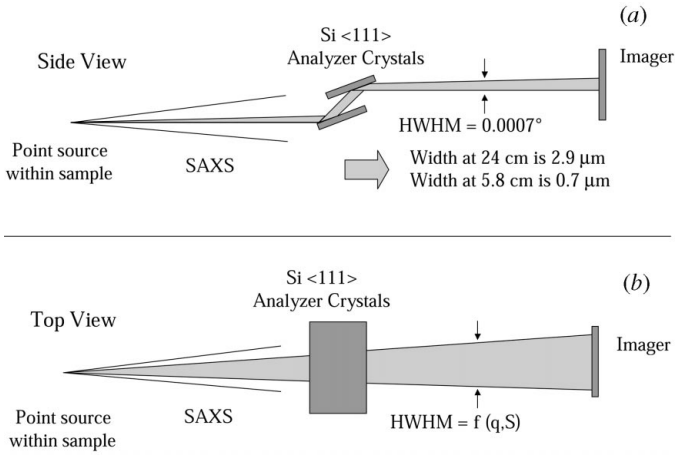

Figure 4
Side view (*a*) and top view (*b*) ray diagrams for small-angle-scattered X-rays passing through the analyzer crystals.

HWHM of 1.0 μm at a distance of 5.8 cm. Thus, the spatial resolution of the image is different in the directions perpendicular and parallel to the analyzer crystals. Since the resolution parallel to the crystals is a complicated function of q as well as the shape and orientation of the individual scattering object, we specify the intrinsic spatial resolution of the USAXS image to be the HWHM of the PSF in the direction perpendicular to the analyzer crystals (the actual resolution may be less than this depending upon the imaging system used). Using Si optics and a photon energy of 8.94 keV, sample-to-detector distances from 24 cm to 5.8 cm have been explored with resulting intrinsic resolutions ranging from 2.9 μm to 0.7 μm. Sample-to-detector distances down to 3.4 cm have been used with ⟨111⟩ Ge analyzer crystals at a photon energy of 17 keV with a resulting intrinsic resolution of 0.5 μm. We emphasize that this intrinsic resolution is not necessarily a measure of the experimentally observed limiting resolution; this limit is usually dominated by inherent limitations in our X-ray camera system, either through the conversion of X-rays to optical light (about 1.2 μm resolution limit) or by the Nyquist frequency of the pixel size (when low-power objective lenses are used).

At larger q ($q \geq 0.0015$ Å^{-1}), the angular spread in the $q_{\|}$ direction becomes considerably larger than in the $q_{\perp}$ direction, an effect that is observed clearly in our larger-q USAXS images. At present, this spreading limits the effectiveness of USAXS imaging at large q and work on reducing this problem is ongoing.

The intensity distribution of an image produced by an extended object is the convolution of the object's inherent shape/intensity distribution and the PSF described above. Thus, a compact object (such as a spherical cavity) that is significantly larger than the intrinsic resolution will exhibit an intensity distribution that is nearly constant, except at its boundary where the intensity drops quickly to zero. By setting the intensity cutoff appropriately, much of the broadening effect can be effectively eliminated in the USAXS images. This effect was examined by making images over a wide range of exposures on high-contrast nuclear emulsion plates. It was found that under-exposing the plate greatly decreases (and nearly eliminates) the spreading effect. The nuclear-emulsion-plate images presented in this paper were exposed in this fashion. As an additional test, multiple images were also obtained using sample-to-detector distances ranging from 24 cm to 5.8 cm. Although the general image quality was improved dramatically by decreasing this distance, the measured sizes of the various scattering objects were insensitive to these changes.

An important imaging artifact is the background produced by the instrument profile function. During non-imaging USAXS experiments, this profile function is measured by conducting a scan with no sample in the beam, thus enabling absolute calibration and allowing the effect of the optics to be explicitly removed during data reduction. In a USAXS image of a weakly scattering sample, this optics background is sometimes visible as bright spots, curved lines, and various other features related to imperfections on the analyzer and collimator crystal surfaces (the optical elements closest to the detector). These artifacts can be readily identified in composite images since they are perfectly repeated in each of the component images. The simplest method for reducing the occurrence of these background features is to use the best surface polishing treatment available and to minimize the 'footprint' of the X-ray beam on the X-ray optics by reducing the number of reflections in the crystal pairs to just two. In our most recent experiments with new analyzer and collimator crystals, all of these imaging artifacts have been successfully eliminated.

All of the above discussion assumes that multiple scattering is negligible. When multiple scattering is significant, it is an issue for radiography, DEI and USAXS imaging. The effects of multiple scattering depend strongly upon many factors, including the severity of the multiple scattering and the possibly heterogeneous position and size distributions of the scatterers within the imaged volume. In general, multiple scattering will cause at least some distortion of the images and this distortion can become so severe as to completely eliminate all useful image data. If multiple scattering is significant, it shows up directly on a USAXS scan of the sample as broadening of the rocking curve compared with the blank scan with no sample. If broadening is not present, then multiple scattering can be safely ignored.

5. Imaging experiments

The following describes several examples of how USAXS imaging can be used. Samples were mostly provided by collaborators who are listed in the acknowledgements. They include: polycrystalline copper deformed under conditions where creep cavities would develop (Dobbyn *et al.*, 1989), and bovine articular cartilage. USAXS images of the copper samples were acquired using nuclear emulsion plates and the cartilage images were obtained using a high-resolution X-ray imaging camera.

The copper samples that were used to explore the USAXS imaging technique were cut from two polycrystalline copper rods with grain diameters of ~0.5 mm. The first rod was deformed at a constant strain rate of 10^{-6} s^{-1} for 1 h at 873 K in a vacuum of 10 mPa. The volume fraction of creep cavities produced was approximately 4.5×10^{-4} as measured by hydrostatic weighing. The second rod was subjected to the same thermal treatment, but was not deformed. One longitudinal (parallel to the tensile axis) and one transverse (perpendicular to the tensile axis) USAXS sample was prepared from each of the two rods, with the undeformed samples serving as controls. Additional details concerning the samples and their preparation may be found in work by Long *et al.* (2001). A photon energy of 8.94 (2) keV (just below the Cu *K* edge) was used to maximize the intensity of the transmitted beam.

USAXS images were obtained with the incident X-ray beam slits positioned to give beam sizes ranging from 0.4×2.4 mm to 0.8×3.2 mm. Images were recorded on nuclear emulsion plates having a grain size of approximately 0.17 μm. The samples and film plates were translated together between exposures, producing composite images up to 3.2×10.4 mm in size. Images were recorded at several q values, ranging from 0 to 0.012 $Å^{-1}$.

Figure 5
USAXS image of creep cavities in Cu, with (*a*) $q = 1.3 \times 10^{-4}$ $Å^{-1}$ and (*b*) $q = 7.5 \times 10^{-4}$ $Å^{-1}$ and the central grain rotated about **q** to a diffracting condition.

USAXS data from each of the four samples were placed on an absolute scale and corrected for slit smearing (Long *et al.*, 1991). Small variations with sample position were observed in the USAXS from the undeformed longitudinal and transverse samples. USAXS imaging demonstrated that this variation came mostly from double Bragg diffraction from opportunistically oriented grains. USAXS scans could only be obtained with integrity from regions devoid of such grains. The scattering intensity from the deformed samples was much greater than that from the undeformed samples due to scattering from the creep cavities in the former. This scattering varied significantly with sample position, indicating that the creep cavities were arranged inhomogeneously over the sampled volume (~0.29 mm^3).

USAXS images from the two undeformed samples are nearly featureless and exhibit no significant differences. USAXS images from the longitudinal and transverse deformed specimens, however, show different views of the cavitation microstructure, with localized clusters of nearly spherical creep cavities visible throughout the sample volume (Long *et al.*, 2001). Low-q (1.3×10^{-4} $Å^{-1}$) transverse images show nearly face-on views of cavity clusters that range in size from about 100 to 600 μm across. The longitudinal images show an edge view of such clusters. The size of the individual cavities varies from a maximum diameter of around 10 μm down to around 5 μm. Images acquired at larger q (7.5×10^{-4} $Å^{-1}$) show clusters of much smaller features (≤3 μm). Stereo USAXS images of these smaller features show that they reside on the sample surfaces, and therefore probably result from the sample preparation.

As mentioned previously, in scattering from a polycrystalline sample, some of the grains may be oriented for Bragg diffraction. A portion of this diffracted intensity can undergo a second Bragg reflection and appear as increased scattering intensity at small angles. Analyzing SAS data that are contaminated by such double Bragg contributions can lead to incorrect results. USAXS imaging offers a simple method for avoiding such problems since double Bragg diffraction shows up clearly on USAXS images as broad darkened regions that are very sensitive to rotation about **q** (unlike small-angle scattering features). Fig. 5(*a*) shows a region of the sample containing a large circular arrangement of cavities. Fig. 5(*b*) shows the same region of the sample after rotating to a local Bragg condition. The intensity from double Bragg diffraction decreases more slowly with increasing q than the Porod scattering from the cavities, so a q of 7.5×10^{-4} $Å^{-1}$ was used to enhance the double-diffraction contrast in this image (at the expense of the cavities). A large irregularly shaped darkened region appears within the circular area enclosed by the creep cavities, thus demonstrating that the enclosed volume is a single grain. The irregular shape of the darkened region is caused by strain fields within the grain, an effect commonly observed in X-ray topographs.

Now let us use the theoretical background presented earlier to interpret two USAXS images of the same volume of the

transverse deformed specimen, acquired at $q = 1.3 \times 10^{-4}$ Å^{-1} and $q = 7.5 \times 10^{-4}$ Å^{-1}. In the $q = 1.3 \times 10^{-4}$ Å^{-1} image shown in Fig. 6(*a*), spherical cavities larger than about $3/q \simeq 2.3$ µm in diameter will be in the Porod regime and cavities smaller than around $1/q \simeq 0.8$ µm will be in the Guinier scattering regime. Since exposure times were kept as short as possible to minimize angular spreading effects, cavities smaller than around 1 µm would not appear in this image. The figure shows a cluster of voids that are approximately 10 µm in diameter. In the $q = 7.5 \times 10^{-4}$ Å^{-1} image of the same scattering volume shown in Fig. 6(*b*), these large voids are not visible. Instead, a large collection of much smaller objects is visible in an immediately adjacent region. As mentioned above, stereo images of these smaller scattering features show that they reside on the sample surfaces. The large cavities do not appear in this image because the exposure times were not scaled by q^{-4} as required for spherical objects, and the features are too under-exposed to appear. The small features visible in Fig. 6(*b*) are therefore not spheres and analysis of images acquired at several q's shows that their shape factors are instead consistent with disks. This information could not have been obtained without analysis of a q series since the spatial resolution is inadequate to show the true shapes of the small scattering features.

Finally, as previously mentioned, composite images allow extended structures to be imaged. Fig. 7 shows a composite USAXS image of an 80 µm thick cross section from another annealed Cu sample that was pre-notched to initiate a mode I ductile crack. The sample was then strained at a rate of 2×10^{-6} for 5 h at a temperature of 873 K. The intrinsic resolution is 0.9 µm and $q = 5.0 \times 10^{-4}$ Å^{-1}. A total of 185 exposures were taken, giving a final image size of 12.5 × 14.8 mm with a total acquisition time of about 30 min. The fine structure that is distributed throughout the image is creep cavities similar to those shown in Figs. 5 and 6.

A bovine cartilage sample is used to demonstrate an extremely useful technique that we refer to as selected-area (SA) USAXS (analogous to selected-area diffraction which is commonly used in TEM). Pinhole SAXS studies of similar cartilage samples were conducted previously and strong SAXS was detected from an unidentified region of the samples (Irving & Muehleman, 2003). Synchrotron X-ray radiography and phase-contrast imaging experiments were attempted but no corresponding structures were observed.

Fig. 8 shows USAXS images from a 1 mm thick bovine cartilage sample held within a wet cell. The images were obtained using ⟨111⟩ Ge analyzer crystals, a photon energy of 17 keV, and a high-resolution (∼1 µm) X-ray camera at a sample-to-detector distance of 10.5 cm. A q of 0.001 Å^{-1} was used. Although the photon energy was above that of the Ge *K* shell, the resulting fluorescence only produced a slight uniform background. The resulting intrinsic resolution of the geometry is 1.5 µm. Most of the sample showed no scattering. However, a broad diffuse band of scattering intensity, shown in Fig. 8(*a*), started approximately 30 µm away from the bone, which appears as the overexposed object in the figure. The diffuse

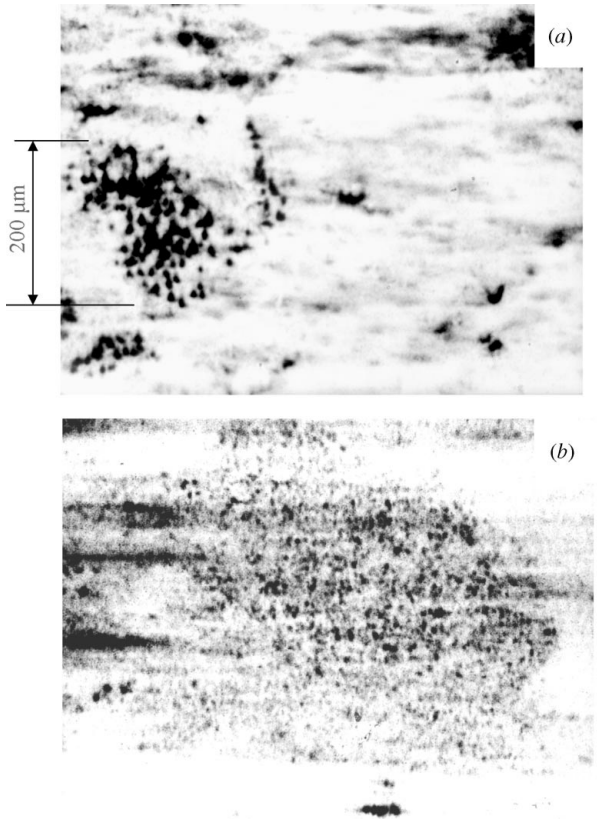

Figure 6
USAXS images of the same region of the sample taken with (*a*) $q = 1.3 \times 10^{-4}$ Å^{-1} and (*b*) $q = 7.5 \times 10^{-4}$ Å^{-1}.

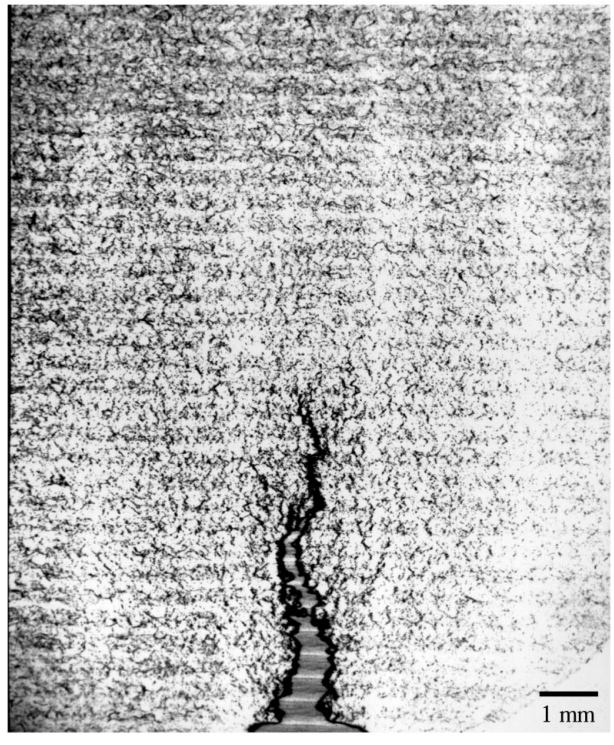

Figure 7
Composite USAXS image of a mode I ductile crack in Cu with $q = 5.0 \times 10^{-4}$ Å^{-1}.

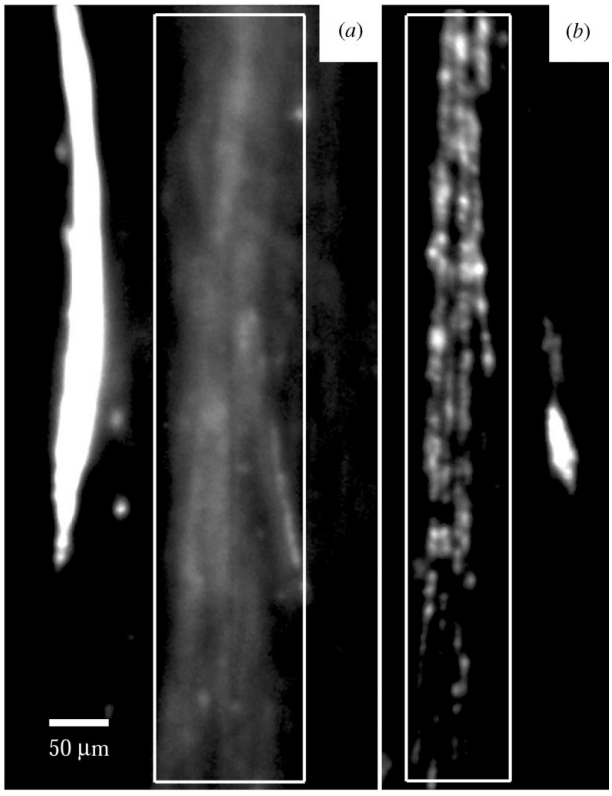

Figure 8
USAXS images of 1 mm thick bovine cartilage in a wet cell showing regions (*a*) near the bone (overexposed object) and (*b*) 400 μm away from the bone. The boxed regions were used to acquire the selected-area USAXS scans shown in Fig. 9. For both images, $q = 0.001$ Å^{-1}.

band was approximately 60 μm across. Our angular filtered parallel-beam monochromatic radiographic images of this same sample volume were completely featureless aside from some well understood beam structure from our collimator optics. Another bovine cartilage sample was examined with the same results. Upon rotating the sample by 90° around the beam axis, the diffuse band disappeared. In the original orientation, approximately 40 μm away from the broad band, the bright string of objects shown in Fig. 8(*b*) was observed. This feature did appear weakly using radiographic imaging. To learn more about the underlying structure responsible for the scattering, the incident-beam slits were moved in so that the beam was restricted to the region indicated by the box in Fig. 8(*a*). This is therefore analogous to the selected-area aperture used in TEM. A USAXS scan was then taken from this selected region of the sample. This same procedure was repeated for the scattering objects shown in Fig. 8(*b*). Fig. 9 shows the desmeared (corrected for slit smearing) SA USAXS scans from the two regions. The scattering from the diffuse band (near bone) region exhibits a pronounced curvature and a terminal slope that is indistinguishable from q^{-4}, indicating the presence of a distribution of objects with sharp boundaries. The disappearance of the scattering feature upon sample rotation is consistent with the underlying structures being fibril bundles oriented perpendicular to the bone. Such bundles are known to occur with this orientation and the size (diameter) distributions are readily obtained from the USAXS curve using a maximum-entropy or a regularization algorithm. Those results will be presented elsewhere. The scattering from the far-from-bone region also exhibits a

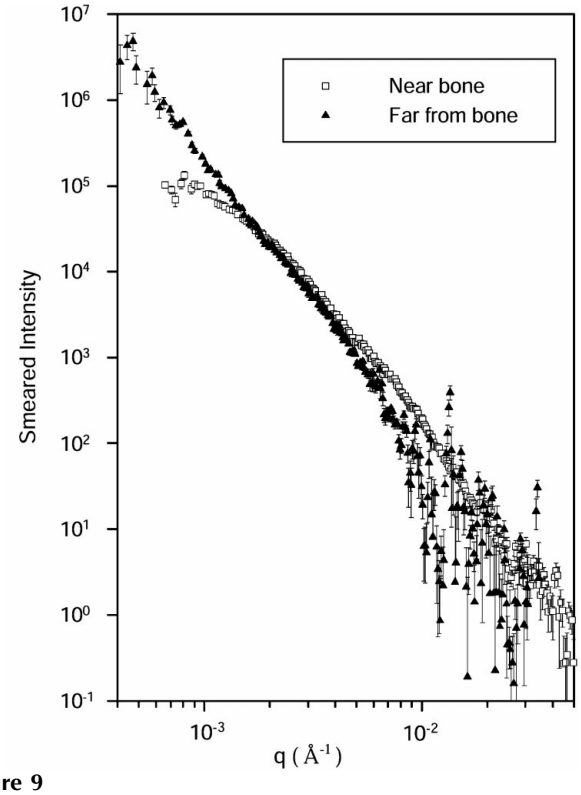

Figure 9
Desmeared selected-area USAXS scans from the boxed regions in Fig. 8.

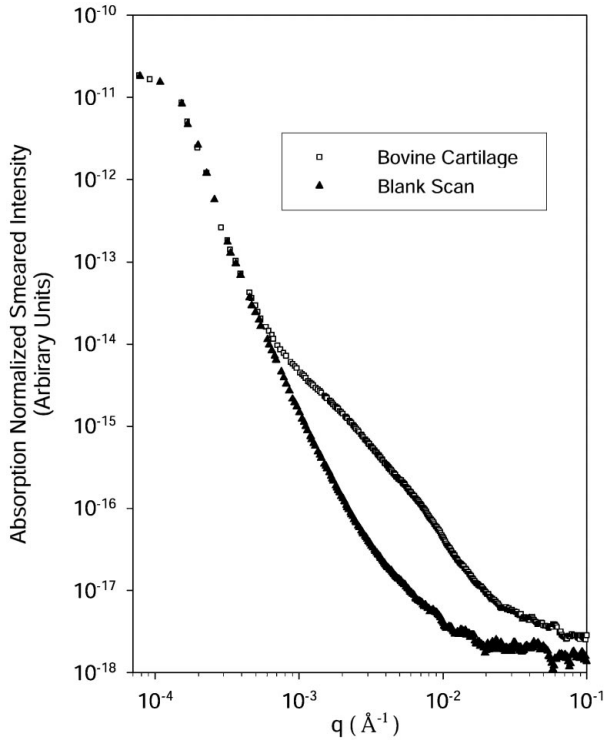

Figure 10
Absorption-normalized slit-smeared USAXS scan from the boxed region in Fig. 8(*a*) along with the corresponding blank scan.

terminal slope of q^{-4}, but the absence of any significant Guinier region makes quantitative interpretation of these data uncertain. Interpretation of these data is ongoing.

Fig. 10 shows the absorption-normalized slit-smeared USAXS data from the broad band feature shown in Fig. 8(*a*) along with the corresponding blank scan. Subtracting these two data sets gives the slit-smeared USAXS data. The SAS begins just before 0.001 Å^{-1}, with an intensity more than three decades below the peak transmitted intensity. This explains why DEI images show no structure from these features. For DEI, the resulting intensity variations amount to less than 0.1% of the peak intensity. For USAXS imaging at 0.001 Å^{-1}, the scattering features are approximately five times our background. USAXS images acquired at smaller q show no features since we also quickly lose sensitivity as the SAS disappears relative to the instrument function background.

6. Conclusions

Using two very dissimilar types of samples, metals and biological tissues, we have demonstrated that USAXS imaging is very sensitive to the microstructural features and it can be used along with USAXS scans to provide substantial quantitative and qualitative information on the morphology and size distributions of the imaged objects. The techniques that have been demonstrated include: using images acquired at different **q**'s to separate objects of different sizes and morphologies; using USAXS imaging to detect scattering sources (double Bragg scattering and surface flaws) that would invalidate a USAXS analysis; composite USAXS images for examining large specimens; and SA USAXS. Three-dimensional spatial information can be obtained using stereo pairs and rotation sequences. Thus, USAXS imaging serves both as a direct imaging technique and as an important adjunct to small-angle scattering generally. In some cases, USAXS provides good contrast when radiography and phase-contrast imaging do not (such as the bovine cartilage samples). In addition to metal and tissue samples, such as those described in this paper, USAXS imaging has been used to study the structure of ceramics, polymers, microelectronics, bone and minerals. It can be used on samples that are single crystals, polycrystalline, composite and amorphous. USAXS imaging is likely to find application to a broad range of materials problems in metal, ceramic, polymer, mineral and biological systems.

We thank the following people for providing us with samples: Richard Fields and Leonard Smith for the copper samples, and Carol Muehleman and Tom Irving for the bovine cartilage. We are also grateful for the help of Jan Ilavsky and Pete Jemian with the experiments. The UNICAT facility at the Advanced Photon Source (APS) is supported by the University of Illinois at Urbana-Champaign, the Oak Ridge National Laboratory, the National Institute of Standards and Technology and UOP LLC. The APS is supported by the US DoE, Office of Science, under contract No. W-31-109-ENG-38.

References

Berk, N. F. & Hardman-Rhyne, K. A. (1985). *J. Appl. Cryst.* **18**, 467–472.
Chapman, D., Thomlinson, W., Johnston, R. E., Washburn, D., Pisano, E., Gmür, N., Zhong, Z., Menk, R., Arfelli, F. & Sayers, D. (1997). *Phys. Med. Biol.* **42**, 2015–2025.
Davis, T. J. (1994). *Acta Cryst.* A**50**, 686–690.
Davis, T. J. (1996). *J. X-ray Sci. Technol.* **6**, 317–342.
Davis, T. J., Gao, D., Gureyev, T. E., Stevenson, A. W. & Wilkins, S. W. (1995). *Nature (London)*, **373**, 595–598.
Dobbyn, R. C., Farris, J., Harlow, D. G., Delph, T. J. & Fields, R. J. (1989). *Scr. Met.* **23**, 621–623.
Fitzgerald, R. (2000). *Phys. Today*, **53**, 22–23.
Guinier, A. & Fournet, G. (1955). *Small Angle Scattering of X-rays*. New York: Wiley.
Hecht, E. & Zajac, A. (1979). *Optics*. Reading, Massachusetts: Addison-Wesley.
Ilavsky, J., Jemian, P., Allen, A. J. & Long, G. G. (2004). In *AIP Conference Proceedings*, Vol. 705, *Synchrotron Radiation Instrumentation: Eighth International Conference*, edited by T. Warwick, J. Arthur, H. A. Padmore & J. Stöhr. College Park: American Institute of Physics.
Irving, T. C. & Muehleman, C. (2003). Private communication.
Long, G. G., Jemian, P. R., Weertman, J. R., Black, D. R., Burdette, H. E. & Spal, R. (1991). *J. Appl. Cryst.* **24**, 30–37.
Long, G. G., Levine, L. E. & Fields, R. J. (2001). *Mater. Sci. Eng. A*, **309–310**, 28–31.
Rayleigh, L. (1911). *Proc. R. Soc. A*, **84**, 25–46.
Windsor, C. G. (1988). *J. Appl. Cryst.* **21**, 582–588.